

# Minimum weighted norm wavefield reconstruction for AVA imaging

Mauricio D. Sacchi\* and Bin Liu

Department of Physics, University of Alberta, Abadh Bhatia Physics Laboratory, Edmonton, T6G 2J1, Alberta, Canada

Received June 2004, revision accepted April 2005

## ABSTRACT

Seismic wavefield reconstruction is posed as an inversion problem where, from inadequate and incomplete data, we attempt to recover the data we would have acquired with a denser distribution of sources and receivers. A minimum weighted norm interpolation method is proposed to interpolate prestack volumes before wave-equation amplitude versus angle imaging.

Synthetic and real data were used to investigate the effectiveness of our wavefield reconstruction scheme when preconditioning seismic data for wave-equation amplitude versus angle imaging.

## INTRODUCTION

Robust inversion of prestack seismic data is an important step towards the estimation of rock properties and fluid indicators. Recent developments have demonstrated that wave-equation amplitude versus angle (AVA) imaging is an emerging and powerful methodology for the accurate estimation of AVA gathers (Mosher, Foster and Hassanzadeh 1997; Prucha, Biondi and Symes 1999). It is well known that wave-equation imaging methods require regularly acquired wavefields. In order to maximize the benefits of wave-equation AVA imaging when working with irregularly sampled data, Kuehl and Sacchi (2003) and Wang, Kuehl and Sacchi (2003) proposed least-squares migration methods to account for missing observations in the prestack volume. A more economical alternative entails the reconstruction of the acquired wavefield before wave-equation AVA imaging. In this case, the interpolation/resampling problem can be posed as an inversion problem where, from inadequate and incomplete data, an attempt is made to recover a properly sampled version of the original seismic wavefield. The problem, however, is underdetermined and, as is well known, the solution is not unique. Missing observations lie in the null space of the sampling operator and therefore a regularization strategy is required to retrieve a unique and stable data reconstruction. Regularization methods are used not only to retrieve stable

and unique data reconstructions but also to impose desirable features on the spectrum of the reconstructed wavefield. For example, minimum norm spectral regularization can be used when we assume that seismic data are band-limited in the spatial wavenumber domain (Cary 1997; Duijndam, Schonewille and Hindriks 1999; Hindriks and Duijndam 2000). Similarly, a regularization derived using the Cauchy criterion can be used to obtain a high-resolution (sparse) discrete Fourier transform that can be used to perform the synthesis of the data at new spatial positions (Sacchi, Ulrych and Walker 1998; Zwartjes and Duijndam 2000). In the minimum weighted norm interpolation (MWNI) method (Liu and Sacchi 2001, 2003), we have used a spectral weighted norm regularization term that incorporates *a priori* knowledge of the energy distribution of the signal to be interpolated. The technique can be used to interpolate large portions of data simultaneously, along any number of spatial dimensions. It is important to stress that the MWNI algorithm is quite efficient; the computational cost of the interpolation relies on fast Fourier transforms (FFTs) in conjunction with a preconditioned conjugate-gradient scheme to accelerate convergence.

We present examples that illustrate the application of the MWNI algorithm to 2D/3D prestack seismic data regularization. We also test the effectiveness of our interpolation strategy at the time of reconstructing data before 2D/3D wave-equation AVA imaging (Mosher *et al.* 1997; Prucha *et al.* 1999). It is important to stress that rather than performing the classical comparison of data before and after interpolation, we have preferred to compare migrated images

---

\*E-mail: sacchi@phys.ualberta.ca

and to extract AVA curves obtained from common-image gathers before and after interpolation.

Interpolation strategies based on prediction error filters have been shown to yield excellent results in problems where there is enough information to predict the missing data properly (Claerbout 1991; Spitz 1991). However, prediction error filters are unable to handle situations where there are large gaps in the data. In this case, methods that exploit data multidimensionality should be preferred. The type of algorithm proposed in this paper can handle large segments of missing information by using spatial data from as many coordinates as possible.

In the first part of this paper, we introduce the interpolation problem as an inverse problem where a wavenumber-domain norm is used to regularize the inverse problem. Then we briefly review the problem of estimating AVA gathers using wave-equation migration methods. The final part of the paper is devoted to numerical and real data examples. We first examine the 2D problem with a simple synthetic model and with the Marmousi model. Then the 3D reconstruction problem is studied with a simple 3D synthetic data set and a field data set from the Western Canadian Sedimentary Basin. These examples are used to highlight the strengths of our algorithm when preconditioning data for wave-equation AVA imaging.

## PROBLEM FORMULATION

The multidimensional or  $N$ -dimensional (ND) interpolation is carried out along the vector of spatial coordinates  $\mathbf{u}$  for each temporal frequency  $\omega$ . In other words, we denote the seismic data at one monochromatic temporal frequency component as  $D(\mathbf{u}, \omega)$ , where, for instance,  $\mathbf{u} = [x_s, x_r]$  denotes a 2D data volume defined in terms of source and receiver positions; similarly,  $\mathbf{u} = [m_x, m_y, h_x]$  defines a constant azimuth 3D data volume in terms of the two midpoint positions  $m_x, m_y$  and the in-line offset  $h_x$ . It should be remembered that ND refers to the number of spatial dimensions of the reconstruction problem. The methodology presented in this paper can be easily adapted to handle the following cases:

- $N = 1$  : interpolation of one single gather;
- $N = 2$  : prestack 2D interpolation or 3D post-stack interpolation;
- $N = 3$  : interpolation of 3D prestack common-azimuth volumes;
- $N = 4$  : full spatial interpolation (multi-azimuth interpolation).

The multidimensional wavefield  $D(\mathbf{u}, \omega)$  at a monochromatic frequency component  $\omega$  can be organized via lexicographic

ordering in a length- $M$  vector  $\mathbf{x} = [x_1, x_2, \dots, x_M]^T$ . The vector  $\mathbf{x}$  defines the desired observations on the regular grid. The actual observations (recorded data) are given by the elements of the vector  $\mathbf{y} = [x_{n(1)}, x_{n(2)}, x_{n(3)}, \dots, x_{n(N)}]^T$ , where the set  $\mathcal{N} = \{n(1), n(2), n(3), \dots, n(N)\}$  is used to indicate the position of the known samples or observations in the regular grid. It is clear that with this type of sampling, one is assigning recorded traces to the nearest spatial position in the desired grid (binning). We now define the sampling matrix  $\mathbf{T}$  with elements  $T_{i,j} = \delta_{n(i),j}$ , where  $\delta$  denotes the Kronecker operator. It is quite simple to show that the complete data and the observations are connected by the following linear system of equations:

$$\mathbf{y} = \mathbf{T}\mathbf{x}. \quad (1)$$

For example, if we assume that the complete data consist of  $M = 5$  consecutive samples  $\mathbf{x} = [x_1, x_2, x_3, x_4, x_5]^T$ , whereas the observations (available data) are given by samples at positions  $\mathcal{N} = \{2, 3, 5\}$ , that is  $\mathbf{y} = [x_2, x_3, x_5]^T$ , then (1) becomes

$$\begin{pmatrix} x_2 \\ x_3 \\ x_5 \end{pmatrix} = \begin{pmatrix} 0 & 1 & 0 & 0 & 0 \\ 0 & 0 & 1 & 0 & 0 \\ 0 & 0 & 0 & 0 & 1 \end{pmatrix} \begin{pmatrix} x_1 \\ x_2 \\ x_3 \\ x_4 \\ x_5 \end{pmatrix}. \quad (2)$$

The complete data  $\mathbf{x}$  can be retrieved by minimizing the cost function,

$$J = \|\mathbf{T}\mathbf{x} - \mathbf{y}\|_2^2 + \mu \mathbf{x}^T \mathbf{Q}^\dagger \mathbf{x}, \quad (3)$$

where the matrix of weights  $\mathbf{Q}^\dagger$  is given by the expression,

$$\mathbf{Q}^\dagger = \mathbf{F}_{\text{ND}}^H \mathbf{\Lambda}^\dagger \mathbf{F}_{\text{ND}}. \quad (4)$$

$\mathbf{F}_{\text{ND}}$  and  $\mathbf{F}_{\text{ND}}^H$  denote the forward and inverse ND Fourier transforms, respectively, and the superscript H is used to indicate the complex conjugate transpose. The band-limiting operator  $\mathbf{\Lambda}^\dagger$  is given by

$$\mathbf{\Lambda}^\dagger(\mathbf{k}) = \begin{cases} [S(\mathbf{k})]^{-1} & \mathbf{k} \in \Omega(\mathbf{k}) \\ 0 & \mathbf{k} \notin \Omega(\mathbf{k}) \end{cases} \quad (5)$$

where  $S(\mathbf{k})$  is the unknown spectral density of the multidimensional prestack data cube at wavenumber element  $\mathbf{k}$ . It is clear that in the above expression, the symbol  $\dagger$  is also used to indicate the pseudo-inverse of the spectral density. We will assume that the data are band-limited. In other words,  $S(\mathbf{k}) = 0$ ,  $\mathbf{k} \in \bar{\Omega}(\mathbf{k})$ , the complement of  $\Omega(\mathbf{k})$ .

The cost function given by (3) is minimized using the method of conjugate gradients. In the numerical implementation we have reduced the cost function to its standard form

(Hansen 1998) and used the so-called *regularization by iteration* method (Hanke 1995). For this purpose, we first define a new variable,

$$\mathbf{x} = \mathbf{W}\mathbf{z}, \quad (6)$$

where  $\mathbf{W} = \mathbf{F}_{\text{ND}}^{\text{H}} \mathbf{\Lambda}^{1/2}$ . It can be shown that the cost function in the standard form becomes

$$J = \|\mathbf{TWz} - \mathbf{y}\|_2^2 + \mu \mathbf{z}^{\text{T}} \mathbf{z}, \quad (7)$$

where the elements of the diagonal form  $\mathbf{\Lambda}^{1/2}$  are given by

$$\Lambda(\mathbf{k}) = \begin{cases} [S(\mathbf{k})]^{1/2} & \mathbf{k} \in \Omega(\mathbf{k}) \\ 0 & \mathbf{k} \notin \Omega(\mathbf{k}) \end{cases}. \quad (8)$$

Equation (7) is solved using conjugate gradients with regularization by iteration (Hanke 1995). This is equivalent to finding the smallest number of iterations  $k$  that satisfies the discrepancy principle,

$$\|\mathbf{TWz}^k - \mathbf{y}\|_2^2 \approx \epsilon, \quad (9)$$

where  $\epsilon$  defines an approximate fitting goal. The conjugate-gradient method (Hestenes and Stiefel 1952) is used to minimize expression (9). In this case we define the following compound operator  $\hat{\mathbf{T}} = \mathbf{TW}$  and proceed with the following conjugate-gradient solver for the variable  $\mathbf{z}$ :

Initialization  $\mathbf{z}_0 = \mathbf{0}$ ;

$$\mathbf{s}_0 = \mathbf{y} - \hat{\mathbf{T}}\mathbf{z}_0 = \mathbf{y}; \quad \mathbf{r}_0 = \mathbf{p}_0 = \hat{\mathbf{T}}^{\text{H}}(\mathbf{y} - \hat{\mathbf{T}}\mathbf{z}_0) = \hat{\mathbf{T}}^{\text{H}}\mathbf{y};$$

$$\mathbf{q}_0 = \hat{\mathbf{T}}\mathbf{p}_0;$$

$$\gamma_0 = (\mathbf{r}_0, \mathbf{r}_0);$$

for  $i = 0$ : *niter*

$$\alpha_{i+1} = \gamma_0 / (\mathbf{q}_i, \mathbf{q}_i);$$

$$\mathbf{z}_{i+1} = \mathbf{z}_i + \alpha_{i+1}\mathbf{p}_i;$$

$$\mathbf{s}_{i+1} = \mathbf{s}_i - \alpha_{i+1}\mathbf{q}_i;$$

$$\mathbf{r}_{i+1} = \hat{\mathbf{T}}^{\text{H}}\mathbf{s}_{i+1};$$

$$\gamma_{i+1} = (\mathbf{r}_{i+1}, \mathbf{r}_{i+1});$$

$$\text{if } \gamma_{i+1} < \text{tol} * \|\mathbf{y}\|_2^2$$

break;

end;

$$\beta_{i+1} = \gamma_{i+1} / \gamma_i;$$

$$\mathbf{p}_{i+1} = \mathbf{r}_i + \beta_{i+1}\mathbf{p}_i;$$

$$\mathbf{q}_{i+1} = \hat{\mathbf{T}}\mathbf{p}_{i+1};$$

end

Note that the matrix-time-vector multiplication steps in the conjugate-gradient algorithm are implemented *on the fly* using  $N$ -dimensional FFTs. In other words, there is no need to construct and save the operator  $\hat{\mathbf{T}}$  as a matrix.

### Estimation of $S(\mathbf{k})$

The algorithm outlined above requires knowledge of the power spectral density of the complete (unknown) data  $\mathbf{x}$ . We propose to bootstrap the spectral density from the available data using the following procedure:

1 Define  $\mathbf{W}$  as an initial multidimensional band-limiting operator (Duijndam *et al.* 1999).

2 Use the conjugate-gradient method to solve  $\mathbf{TWz} \approx \mathbf{y}$ , and obtain an initial reconstruction of the data  $\mathbf{x} = \mathbf{Wz}$ .

3 Re-estimate the spectral density from the reconstructed data  $\mathbf{x}$ , and compute  $W(\mathbf{k})$  using (8).

4 Repeat steps 2 and 3 until convergence is achieved.

The power spectral density is estimated by means of the data periodogram (the squared-amplitude of the Fourier transform of the data) followed by smoothing (Priestly 1981). Smoothing is required to decrease the variance of the periodogram and obtain the power spectral density of the data. At this point, it must be stressed that other methods of spectral analysis could have been used (see e.g. Marple 1987). However, given the fact that we are dealing with multidimensional problems, we preferred the periodogram followed by smoothing since it can be computed efficiently using the FFT.

It is clear that the above algorithm requires an extra iteration to update the spectral density. Fortunately, since the interpolation is always performed at one temporal frequency at a time ( $\omega - x$  type interpolation), we found that the power spectral density used to interpolate the spatial signal at temporal frequency  $\omega$  can be derived from already interpolated data at frequency  $\omega - \Delta\omega$ . All our examples were computed with this strategy. Note that Hugonnet, Herrmann and Ribeiro (2001) described a similar scheme to estimate the weights required by the high-resolution Radon transform.

### WAVE EQUATION AVA IMAGING

We briefly describe the methodology used to estimate angle-domain common-image gathers. Recorded 2D and 3D data are first organized in the midpoint–offset ( $\mathbf{m}-\mathbf{h}$ ) domain. The measured data at the surface ( $z = 0$ ) is downward continued recursively using the double-square-root operator (Claerbout 1985). Once the complete wavefield has been reconstructed within the target volume, the imaging condition is applied to

compute the subsurface *structural image*. This procedure can be summarized by the following workflow:

$$\begin{aligned} \text{Downward Continuation: } P(\omega, \mathbf{m}, \mathbf{h}, z + \Delta z) \\ &= \mathcal{DSR} P(\omega, \mathbf{m}, \mathbf{h}, z), \\ \text{Imaging: } I(\mathbf{m}, z) &= \mathcal{I}P(\omega, \mathbf{m}, \mathbf{h}, z), \end{aligned}$$

where  $\mathcal{I}$  synthesizes the imaging condition as an operator that entails integration over frequency and offset. The application of this method to 3D migration involves a fairly demanding computational task. It is also clear that regularly sampled data along the offset and midpoint vectors ( $\mathbf{m} = (m_x, m_y)$  and  $\mathbf{h} = (h_x, h_y)$ ) is required. Biondi and Palacharla (1996) presented a reformulation of the double-square-root operator that is valid for common-azimuth data. This method permits 3D data to be handled in a more efficient manner. In this case, the double-square-root downward operator requires 3D FFTs rather than 4D FFTs per frequency slice, like the more demanding full double-square-root operator.

The procedure outlined above is only valid for computing structural images of the subsurface. In order to estimate angle-dependent gathers, we combine common-azimuth double-square-root downward continuation with a ray-parameter-domain imaging transformation (Mosher *et al.* 1997; Prucha *et al.* 1999; Kuehl and Sacchi 2003):

$$\begin{aligned} \text{Downward Continuation: } P(\omega, \mathbf{m}, h_x, z + \Delta z) \\ &= \mathcal{DSR}_{CA} P(\omega, \mathbf{m}, h_x, z), \\ \text{Imaging: } I(\mathbf{m}, p_{h_x}, z) &= \mathcal{A}P(\omega, \mathbf{m}, h_x, z), \end{aligned}$$

where  $\mathcal{A}$  synthesizes the slant-stack operator (summation along lines of constant ray parameter  $p_{h_x} = k_{h_x}/\omega$ ).

It is clear that spatial interpolation is needed to render the data to a form that makes Fourier methods applicable. In our examples we have utilized the MWNI method to resample the data to a regular geometry before double-square-root (common-azimuth) AVA imaging. Rather than attempting to interpolate the data before migration, Wang *et al.* (2003) used least-squares migration to *fit* the migrated image to the observations (recorded traces).

Finally, it is important to stress that the resulting gathers in the midpoint–offset ray-parameter domain can be transformed to angle-domain common-image gathers by a simple expression (Prucha *et al.* 1999),

$$p_{h_x} = \frac{2 \sin(\theta) \cos(\phi)}{c(z, \mathbf{m})},$$

where  $\theta$  is the angle of incidence,  $\phi$  denotes the structural dip in the in-line direction and  $c(z, \mathbf{m})$  is the migration

velocity. Note that with the aid of the above expression  $p$ -gathers can be converted to angle-gathers for subsequent AVA analysis.

## EXAMPLES

### 2D synthetic data set

We first test our algorithm on a simple, horizontally layered model. The horizontally layered model consists of four reflecting interfaces. The acoustic model parameters, in terms of compressional velocities and densities, range from 1900 m/s to 2500 m/s and from 1.6 g/cm<sup>3</sup> to 2.25 g/cm<sup>3</sup>, respectively. All interfaces are well separated. A ray-tracing technique is used to generate the synthetic data set. The ray-tracer takes advantage of the fact that, in a stratified medium, the ray parameter is constant for a particular ray. The geometrical spreading has been calculated assuming a cylindrical wavefront resulting in a  $1/\sqrt{r}$  amplitude scaling, where  $r$  is the distance travelled by the ray. Note that transmission losses are neglected in the synthetics. In Fig. 1(a), we show the common-midpoint (CMP) data at 750 m, which exhibit a clear amplitude variation versus offset (AVO). The offsets for the CMP range from 0 to 1280 m in increments of 20 m. Figure 1(b) shows the same CMP after randomly removing 90% of the traces. The incomplete CMPs are used as the input for the reconstruction. We first perform a Fourier transform along the time axis. Reconstructions are then carried at temporal frequencies along two spatial (midpoint and offset) coordinates simultaneously. The output offset ranges from 0 m to 1200 m for each CMP in increments of 10 m. Figure 1(c) shows the reconstructed CMP at 750 m using minimum weighted norm interpolation (MWNI). Note that MWNI uses not only the four existing traces in this gather but also all the other traces in the data set. Since the model in this case is flat, global information is a very powerful means of obtaining complete local information.

Next, we migrate the complete, incomplete and reconstructed data sets with a wave-equation double-square-root AVA migration algorithm (Prucha *et al.* 1999; Kuehl and Sacchi 2003). Figures 2(a,b,c) show common-image gathers at 750 m, obtained with the original data, the incomplete data and the reconstructed data, respectively. We have extracted AVA curves for the four reflectors (Figs 3a–d). For all four reflectors, the AVA curves obtained from reconstructed data match the curve obtained from the completed data quite well. In addition, they all agree with the theoretical AVA trend for a large range of angles of incidence.

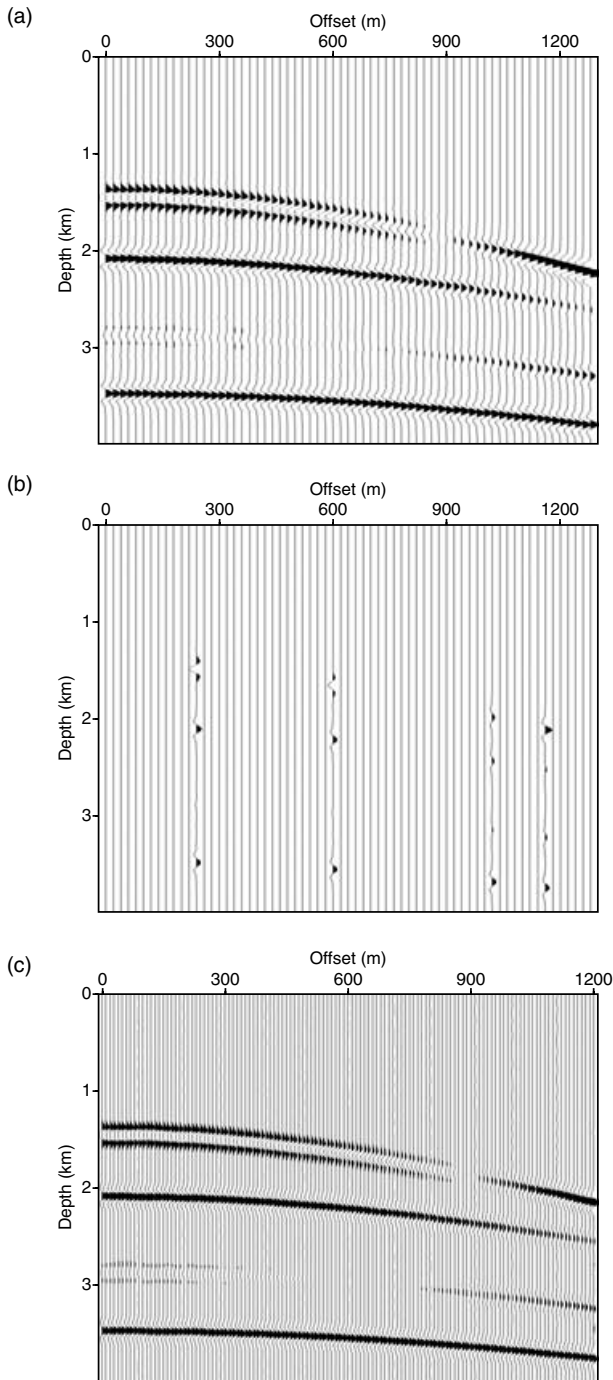


**Figure 1** (a) CMP gather at midpoint position 750 m generated by a ray-tracing code. The program models (cylindrical) geometrical spreading but no transmission effects. The offset for the particular CMP ranges from 0 m to 1280 m in increments of 20 m. (b) The same CMP after randomly removing 90% of the data. (c) The reconstructed CMP using MWNI. The reconstructed offset ranges from 0 m to 1200 m in increments of 10 m.

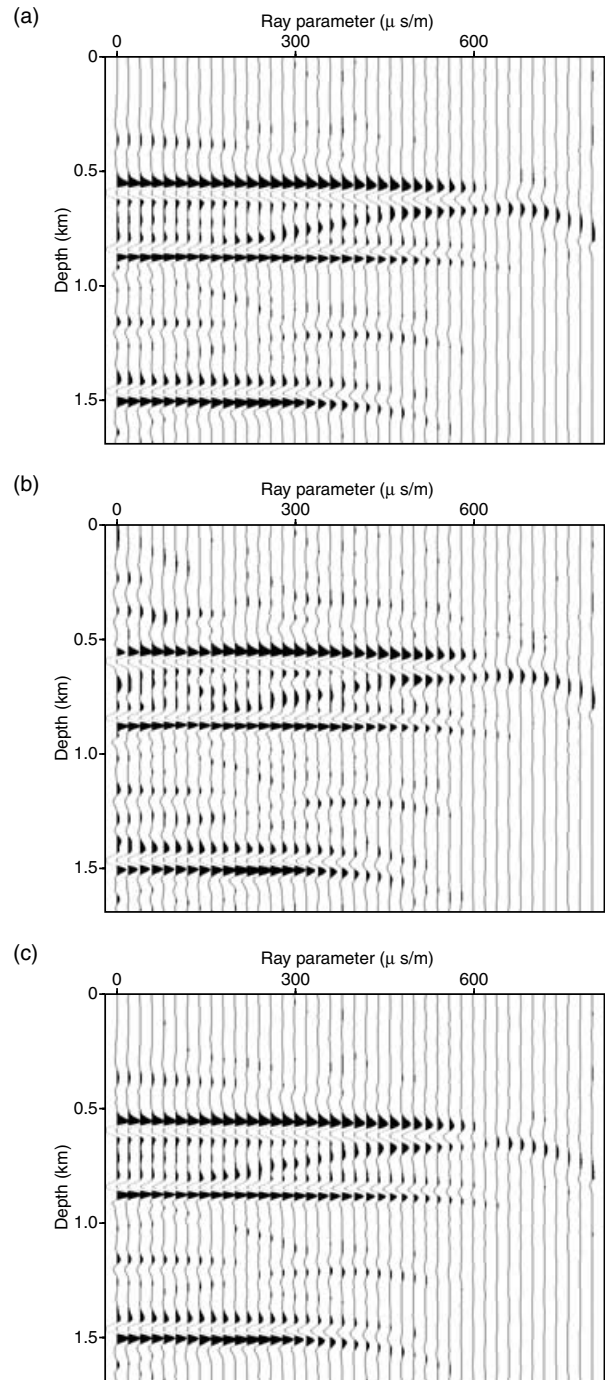


**Figure 2** (a) CIG gather at midpoint 750 m migrated with the original data. (b) The same CIG gather obtained with the incomplete data. (c) The same CIG gather obtained with the reconstructed data.

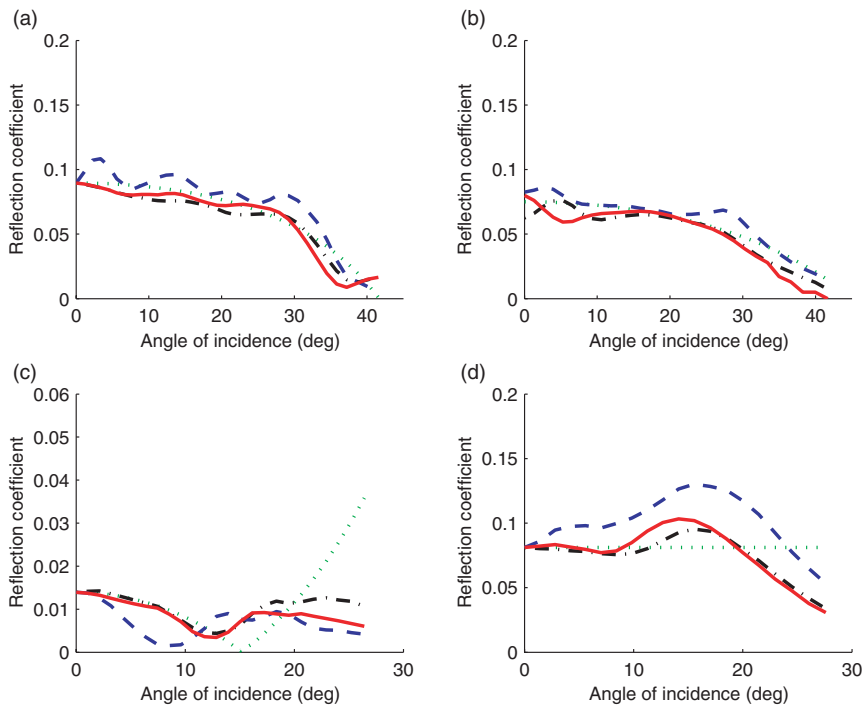


**Figure 3** (a) Theoretical (green/dotted) and extracted AVA curves from the migrated angle gather for the first reflector. Migration with the original complete data (black/dot-dash), incomplete data (blue/dashed), and incomplete data after reconstruction (red/solid). (b) Theoretical and extracted AVA curves for the second reflector. (c) Theoretical and extracted AVA curves for the third reflector. (d) Theoretical and extracted AVA curves for the fourth reflector.

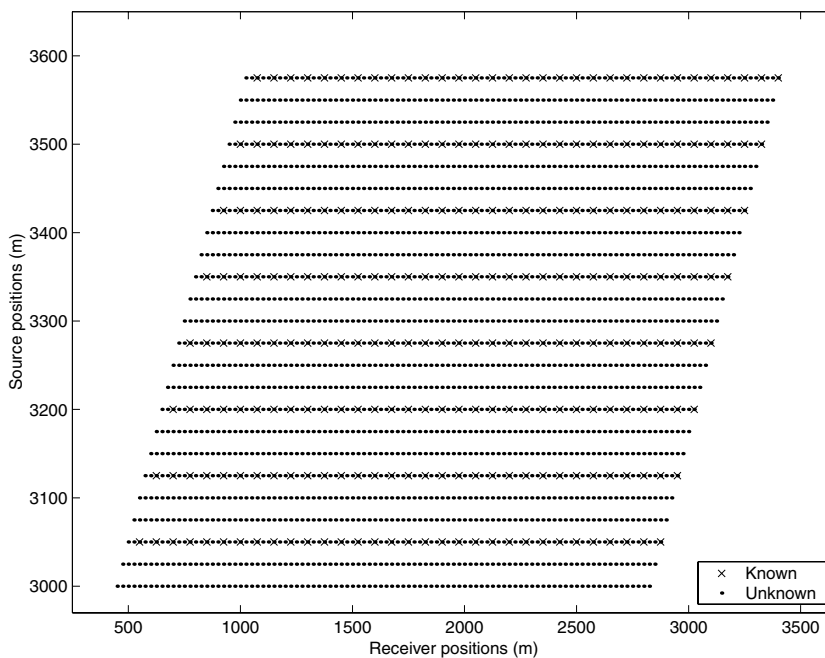


**Figure 4** Source and receiver position map where the crosses indicate the positions of the available traces; the dots indicate the positions to be interpolated.

**Marmousi data set**

The performance of the 2D MWNI algorithm is now demonstrated with the Marmousi data set. The original Marmousi shot and receiver sampling intervals are both 25 m. We simulate a new survey with 75 m shot and receiver intervals. Figure 4 shows a comparison between the original and the

new sampling geometry, where the crosses indicate the positions of available traces and the dots indicate the positions of the traces to be interpolated. The seismic traces from the new survey are the input to our interpolation algorithm. We first transform the data to the frequency domain. Data

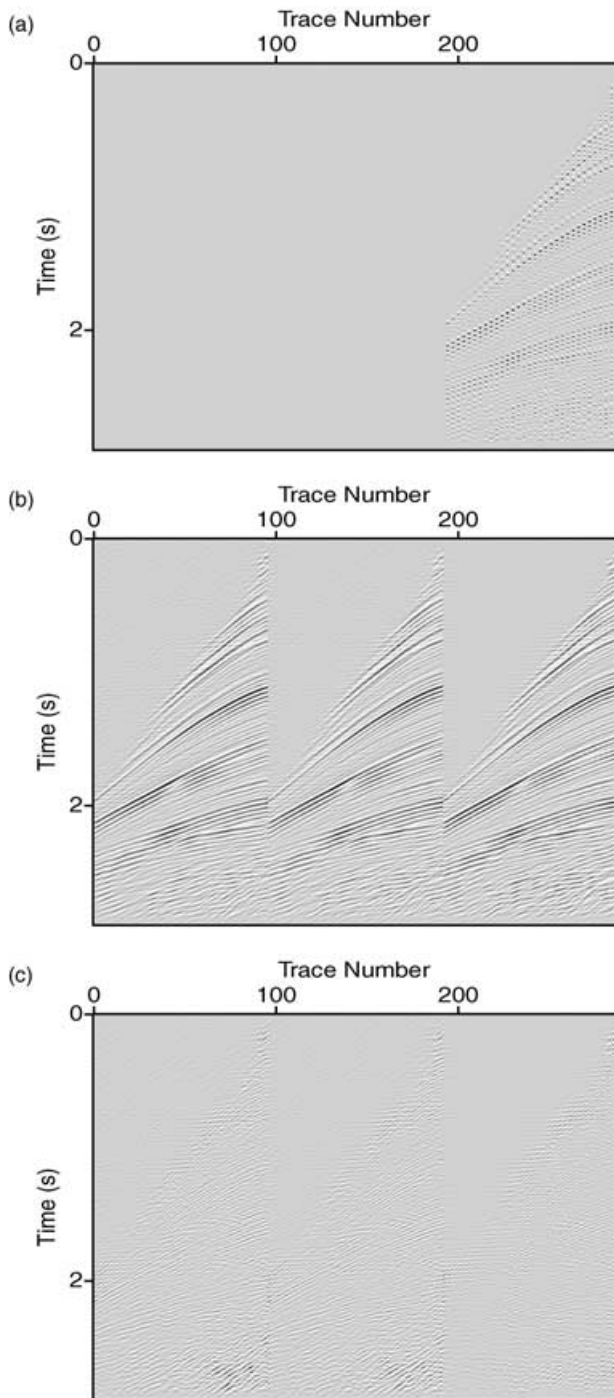


Figure 5 (a) Decimated shot gathers at 3075 m, 3100 m and 3125 m. (b) The reconstructed shot gathers. (c) The reconstruction error.

reconstruction is then carried at each temporal frequency along two spatial (shot and receiver) coordinates simultaneously. All the missing traces have been reconstructed. The data reconstructions at shot positions 3075 m, 3100 m and 3125 m are shown in Figs 5(a,b,c). Figure 5(a) shows the incomplete

shots, Figs 5(b,c) show the reconstructed shot records and reconstruction error, respectively. The  $f$ - $k$  spectra of the original, decimated and reconstructed shot gathers at 3125 m are shown in Figs 6(a,b,c), respectively. Note that the decimated shot gather has been filled with zero traces at the missing trace positions.

We then migrate the complete, incomplete and reconstructed data sets. Figures 7(a-c) show both the stacked image and the migrated common-image gather at CMP location 7500 m using the three different data sets. The migration with the complete data set yields the stacked and common-image-gather images shown in Fig. 7(a). The coarse sampling of the decimated wavefield results in severely aliased events in both the stacked image and the common-image gather (Fig. 7b). In Fig. 7(c), we observe that the migration with the reconstructed wavefield yields an overall better-stacked image without visible signs of aliasing. The continuity of events in the common-image gather is also improved. To study the impact of wavefield interpolation on AVA analysis, a depth point located in the upper half of the model is chosen for AVA inversion. Note that the picked target phase in the common-image gather corresponds to a depth of 880 m in Figs 7(a-c). In Fig. 8, the reflection coefficient based on the acoustic approximation shows an increasing trend with the angle of incidence on the theoretical AVA curve. Despite its roughness, the AVA curve picked on the migrated common-image gathers obtained with the complete data agrees with the theoretical AVA trend. The AVA curve picked on the migrated common-image gather from the reconstructed wavefield is much closer to the original curve, compared with the AVA curve picked on the migrated common-image gather.

In this example the maximum number of conjugate-gradient iterations was set at 30; the algorithm will proceed to reconstruct the next frequency slice if the mean squared error of the reconstruction is below a predefined tolerance or the maximum number of iterations is reached. The tolerance was set at  $1.e-6$ . The reconstruction of the Marmousi data set took 41 minutes using a 1 GHz Pentium III computer.

Finally, we should point out that normal-moveout (NMO) correction could have been used to decrease the spectral bandwidth and therefore stabilize the inversion. However, the Marmousi model is too complex and therefore the NMO correction was not effective in compressing the spatial bandwidth of the data.

### 3D common-azimuth synthetic data set

The MWNI algorithm has also been tested on a 3D common-azimuth synthetic data set. The data set is modelled with a

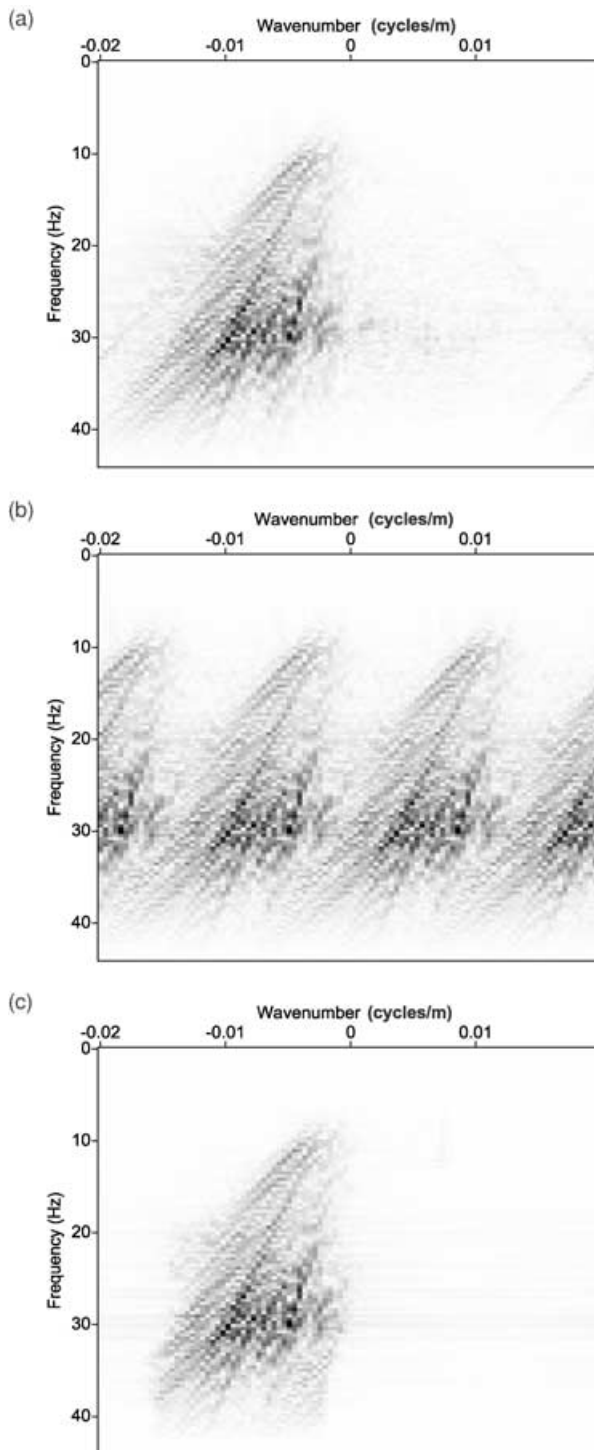


**Figure 6** (a) The  $f$ - $k$  spectrum of the original shot gather at 3125 m. (b) The  $f$ - $k$  spectrum of the same shot gather after decimation (note that the missing data after decimation have been filled with zero traces). (c) The  $f$ - $k$  spectrum of the same shot gather after interpolation.

constant (compressional) velocity model ( $v = 2500$  m/s). The density model consists of a single interface where the densities above and below the interface are  $1.7$  g/cm<sup>3</sup> and  $2.0$  g/cm<sup>3</sup>, respectively. A ray-tracing technique is used to generate the synthetic data set. The geometrical spreading has been calculated assuming a spherical wavefront, resulting in a  $1/r$  amplitude scaling where  $r$  is the distance travelled by the ray. The synthetic data includes a total of 40 cross-line CMPs and 301 in-line CMPs. The cross-line and in-line CMP intervals are 10 m and 5 m, respectively. The CMPs have a non-uniform distribution of offsets ranging from 0 to 1000 m. Figure 10(a) shows a CMP at position (in-line 750 m, cross-line 30 m). The amplitude variation is due to the geometrical spreading effect only. Ninety per cent of the traces in the synthetic data set have been randomly removed. (The incomplete CMP at the same position is shown in Fig. 10(b).) The offset distribution in each CMP bin of the incomplete data is illustrated in Fig. 9. The incomplete data are used as the input for the reconstruction. We first perform a Fourier transform along the time axis. Reconstructions are then carried at temporal frequencies along three spatial coordinates (cross-line CMP, in-line CMP and offset), simultaneously. The reconstructed offset ranges from 0 m to 1000 m in increments of 10 m. Figure 10(c) shows the reconstructed CMP at the same position using MWNI.

Next, we migrate the complete, incomplete and reconstructed data sets with our 3D common-azimuth wave-equation double-square-root AVA migration algorithm. The stacked images for cross-line CMP 30 m (in-line CMP ranges from 750 m to 1000 m), obtained with the original data, incomplete data and reconstructed data, are shown in Figs 11(a,b,c), respectively. Note that both Figs 11(a and c) show uniform reflection strength at the target reflector. In Figs 12(a-c), we show common-image gathers at (in-line CMP 750 m, cross-line CMP 30 m), obtained with the original data, incomplete data and the reconstructed data, respectively. We have extracted AVA curves for the reflector from the above common-image gathers (Fig. 13). Note that the AVA curve obtained from incomplete data (Fig. 13b) does not agree with the theoretical AVA trend. The AVA curve obtained from the reconstructed data (Fig. 13c) matches the one obtained from original data (Fig. 13a) and agrees with the theoretical AVA trend for a large range of angles of incidence.

### 3D common-azimuth field data: Erskine (WCSB)

Finally, we applied the MWNI prestack interpolation to a 3D real seismic data set. The data were obtained from a 3D survey

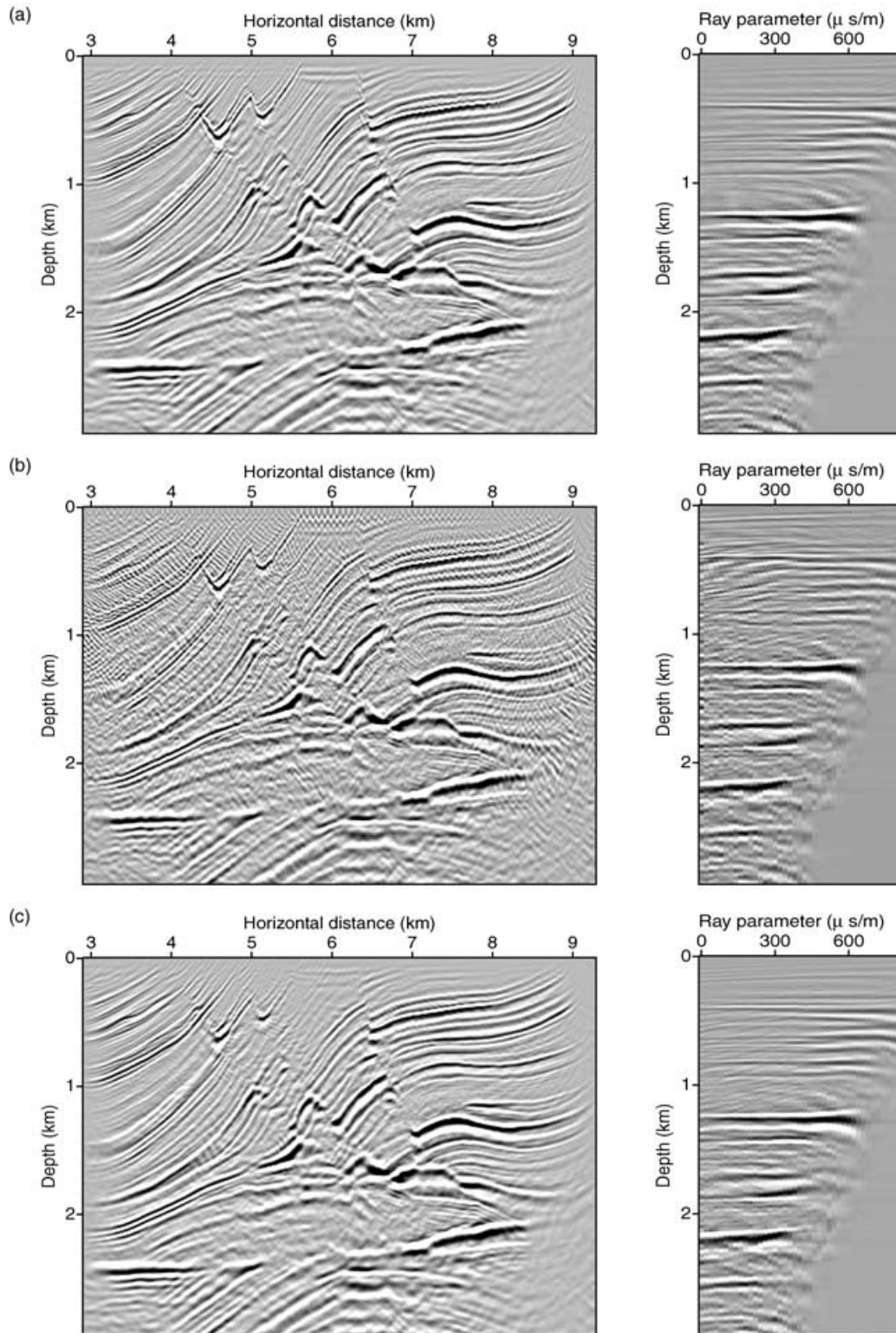


**Figure 7** (a) Migrated image of the Marmousi model and common-image gather at CMP location 7500 m. All the data were used in the migration. (b) Migration of the Marmousi model using the decimated data. (c) Migration of the Marmousi model using the reconstructed data.

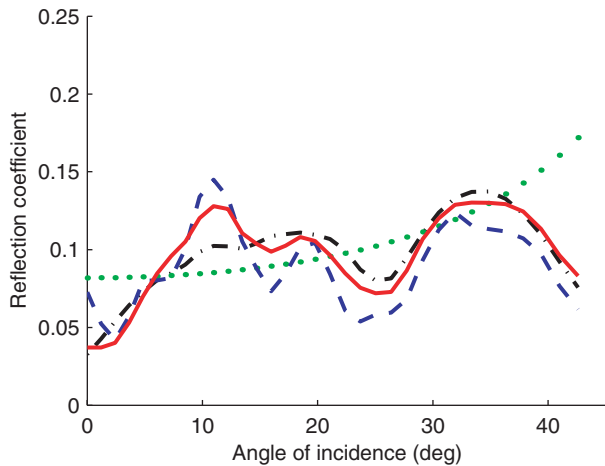


**Figure 8** (a) Theoretical (green/dotted) and extracted AVA curves from the migrated angle gather (black/dot-dash: original complete data; blue/dashed: decimated data; red/solid: data after reconstruction).

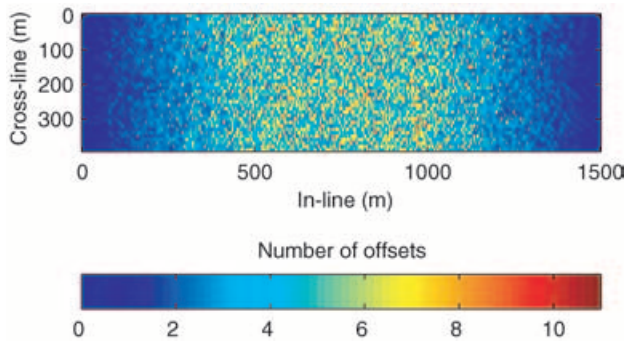


**Figure 9** Distribution of offsets for the 3D field data used to test our interpolation algorithm.

carried out in the Erskine (Alberta) area in the Western Canadian Sedimentary Basin (WCSB). The complete data set contains 150 in-lines and 40 cross-lines with offsets aligned along the in-line direction. The offset distribution in each CMP bin is illustrated in Fig. 14. Figure 15(a) shows the sparse sampling geometry in the cross-line midpoint–offset for in-line #6 (only parts of the cross-line midpoints are shown) and Fig. 15(b) shows the spatial positions after interpolation. Prestack interpolation is applied simultaneously along three dimensions, namely: in-line midpoint, cross-line midpoint and offset. Figure 16(a) shows the original CMPs for in-line #6 and cross-lines #15–18. The reconstructed result is shown in Fig. 16(b). Note that all the gaps have been filled.

3D common-azimuth wave-equation double-square-root AVA migration is applied to both the original and interpo-

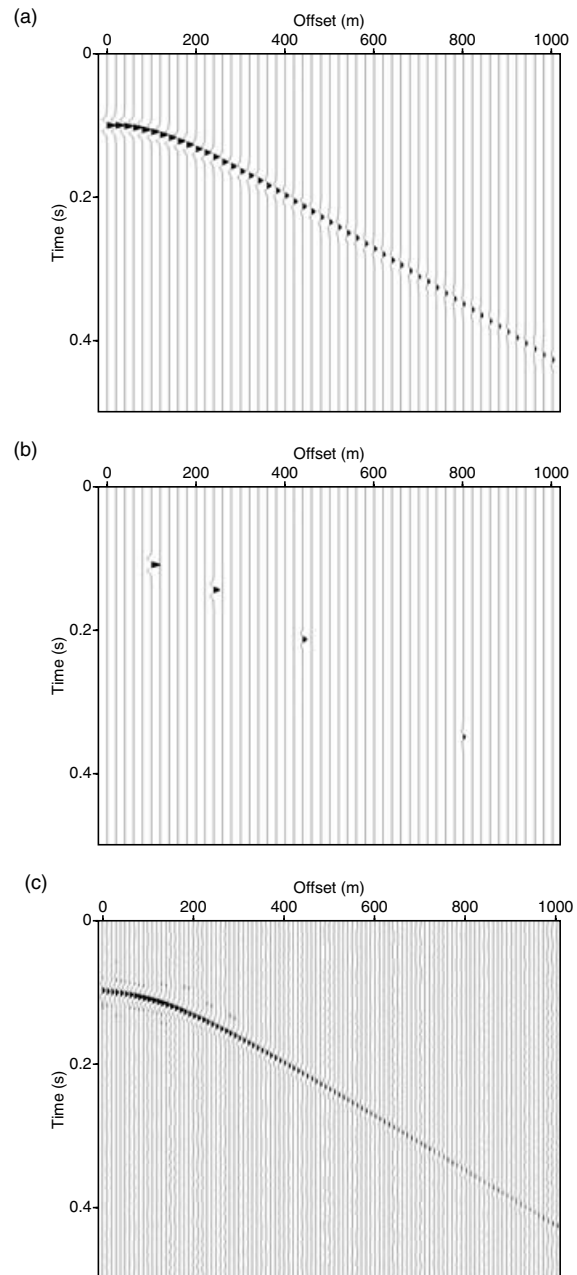


**Figure 10** The CMP at position (in-line 750 m, cross-line 30 m) of (a) the original data, (b) the incomplete data and (c) the reconstructed data.

lated data sets. Figures 17(a,b) show the migrated images for cross-line #36 and in-line #71; in both cases, data before interpolation were used in the migration. Note that the irregular and sparse data sampling results in images of poor quality. Migrated images obtained with the interpolated data are

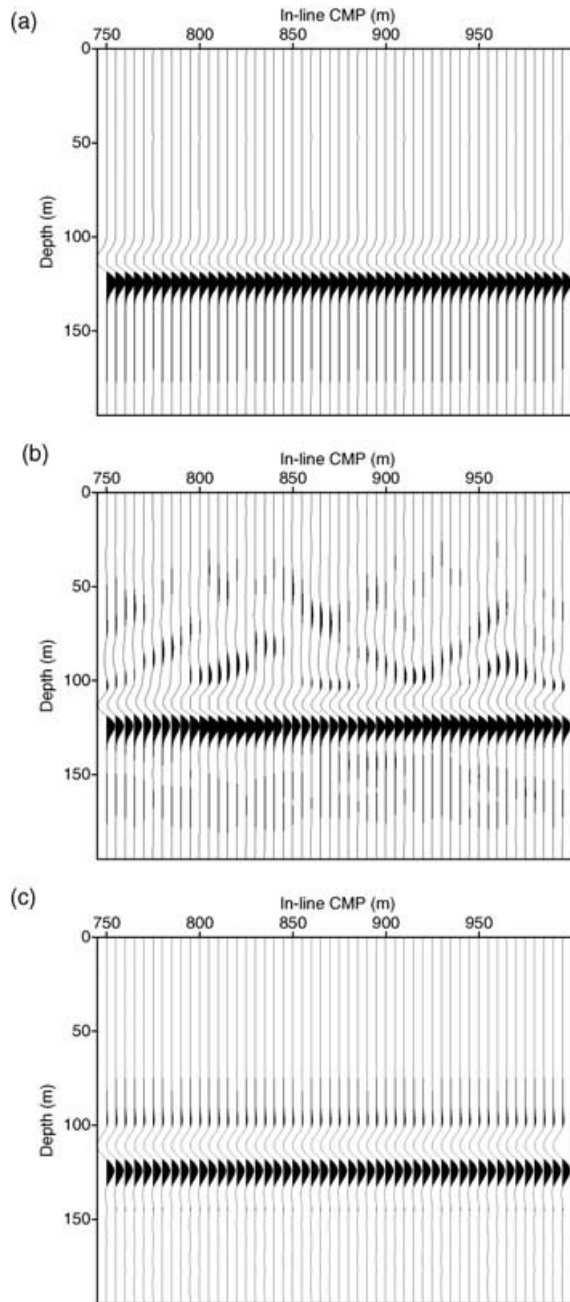


Figure 11 The stacked image for cross-line 30 m obtained with (a) the original data, (b) the incomplete data and (c) the reconstructed data.

shown in Figs 17(c,d). The impact of interpolation before AVA imaging can also be seen in the ray-parameter common-image-gather domain. Common-image gathers for cross-line #36 and in-line #71 are shown in Figs 18(a and b), respectively. The migration with the interpolated data as input yields a common-

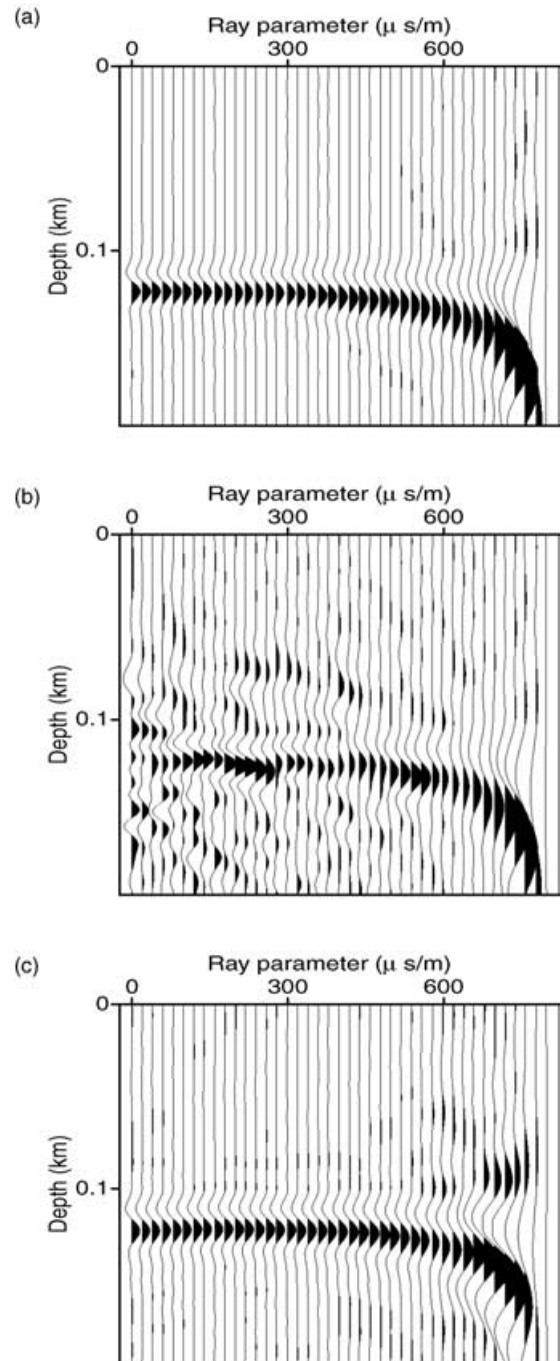
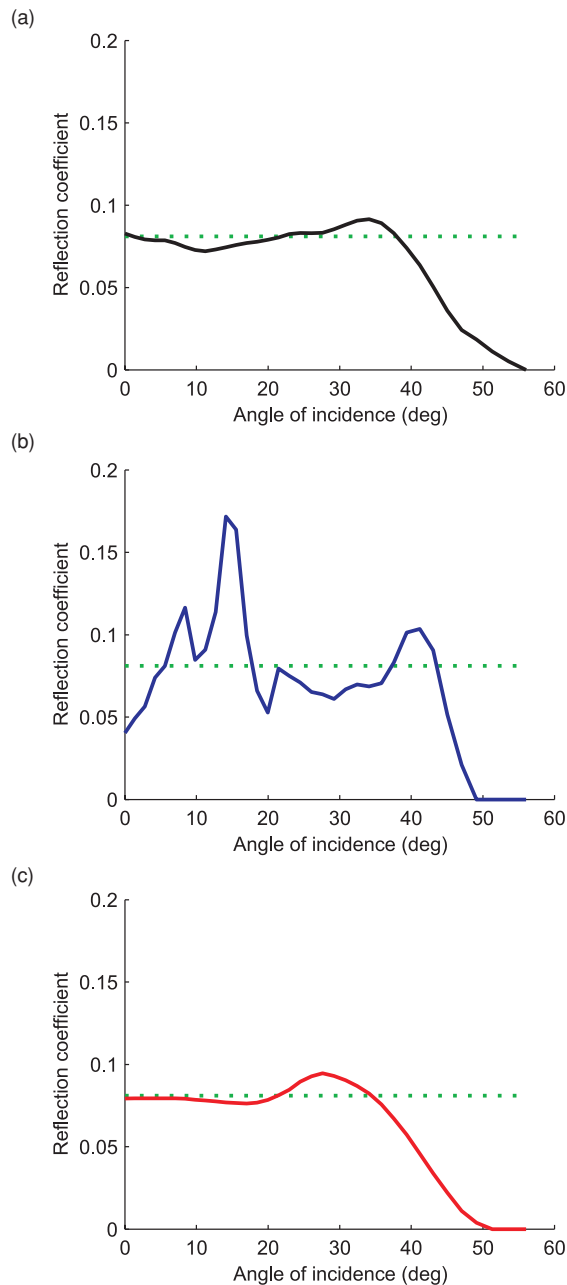


Figure 12 The migrated common-image gather at position (cross-line 30 m, in-line 750 m) obtained with (a) the original data, (b) the incomplete data and (c) the reconstructed data.

image gather (Fig. 18b) with reduced artefacts and better event continuity.

Again, we would stress that although a single cross-line is shown, most of the information necessary to create the missing



**Figure 13** The AVA curves extracted from the migrated CIG at position (cross-line 30 m, in-line 750 m) obtained with (a) the original data, (b) the incomplete data and (c) the reconstructed data.

traces comes from the in-line direction where the data set is more densely sampled. In a standard single-dimension approach, the data would be interpolated first along in-lines and then along cross-lines. The latter would make the interpolation totally dependent on information along the in-line direction. The proposed method, minimum weighted norm interpola-

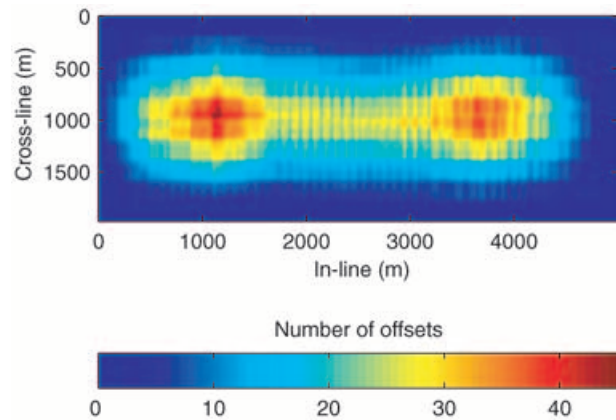


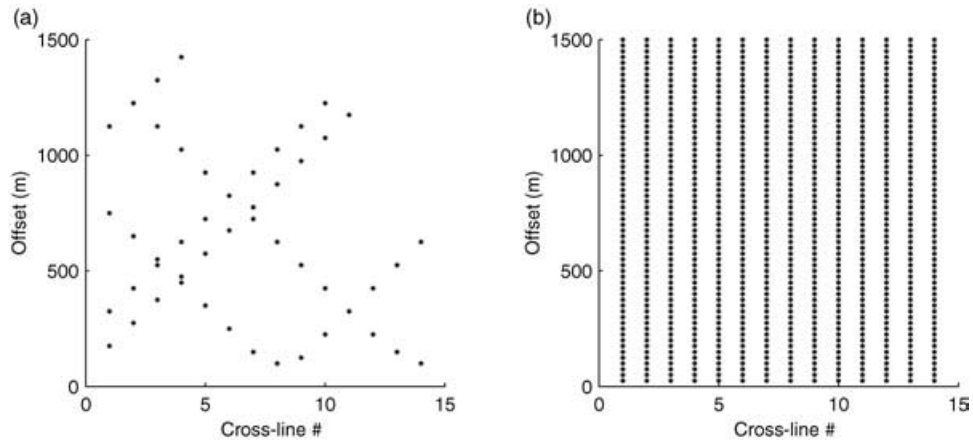
**Figure 14** Distribution of offsets for the 3D field data used to test our interpolation algorithm.

tion, has the capability to combine information from both directions.

## CONCLUSIONS

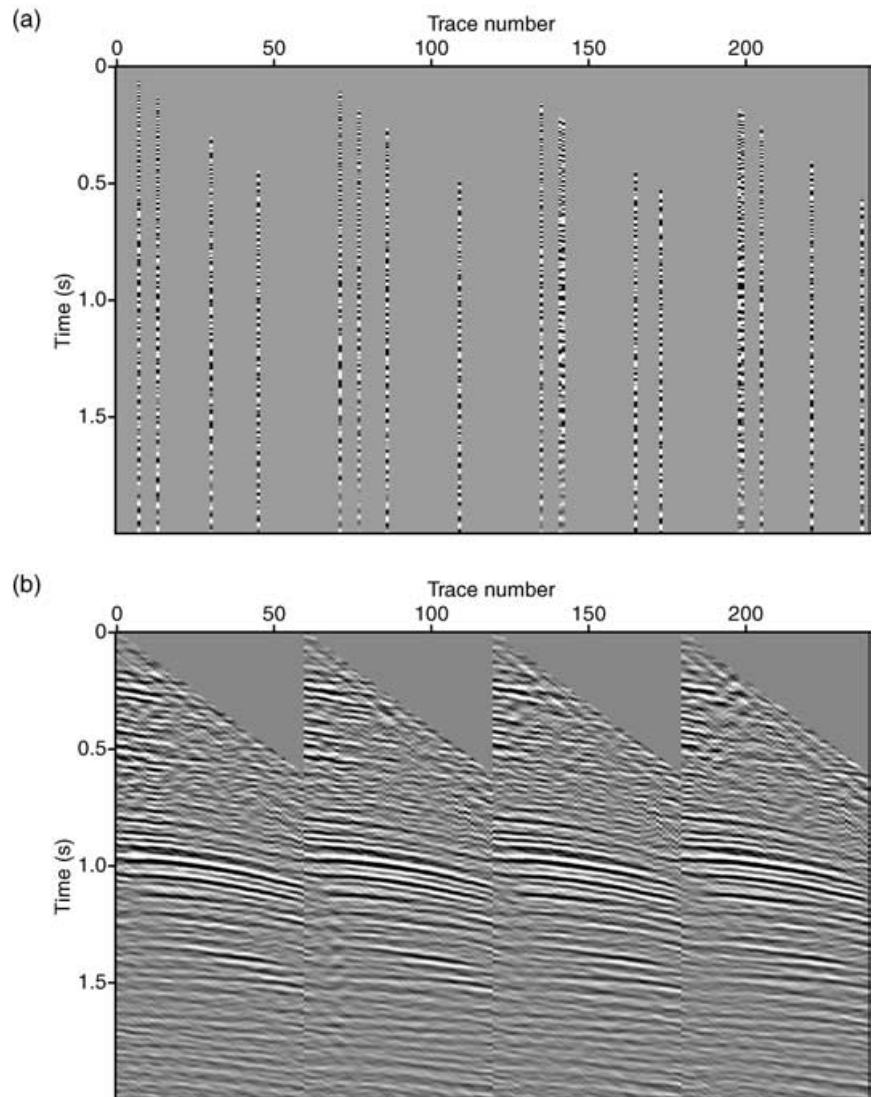
We have applied the MWNI reconstruction algorithm to prestack seismic data before wave-equation AVA migration. The method enables us to incorporate both the band-width and the signal spectrum shape in the interpolation problem and, therefore, it often yields optimal reconstructions. The method is extremely efficient since all computations are carried out via a preconditioned conjugate-gradient algorithm where the computational cost is dominated by the FFT algorithm. It is important to mention that the method can be applied to seismic data in any domain with multiple spatial coordinates. Finally, examples with synthetic and real 3D data show an important reduction of sampling artefacts, both in the stacked image and in individual AVA gathers.

The proposed method can also be implemented using the non-uniform discrete Fourier transform to deal with irregular sampling (Duijndam *et al.* 1999); all the examples shown in this paper have used regular sampling with missing traces. There are many situations where this is applicable. An implementation using non-uniform discrete Fourier transforms could be too expensive to apply in three or four dimensions simultaneously. If the non-uniform discrete Fourier transform were required, a better approach would be to work with individual gathers.



**Figure 15** (a) The map of the incomplete geometry for in-line #6 (note that only parts of the cross-line midpoints are shown). (b) The complete geometry after interpolation for in-line #6.

**Figure 16** (a) The original traces in four adjacent CMPs corresponding to in-line #6 and cross-lines #15–18. (b) CMPs after interpolation.



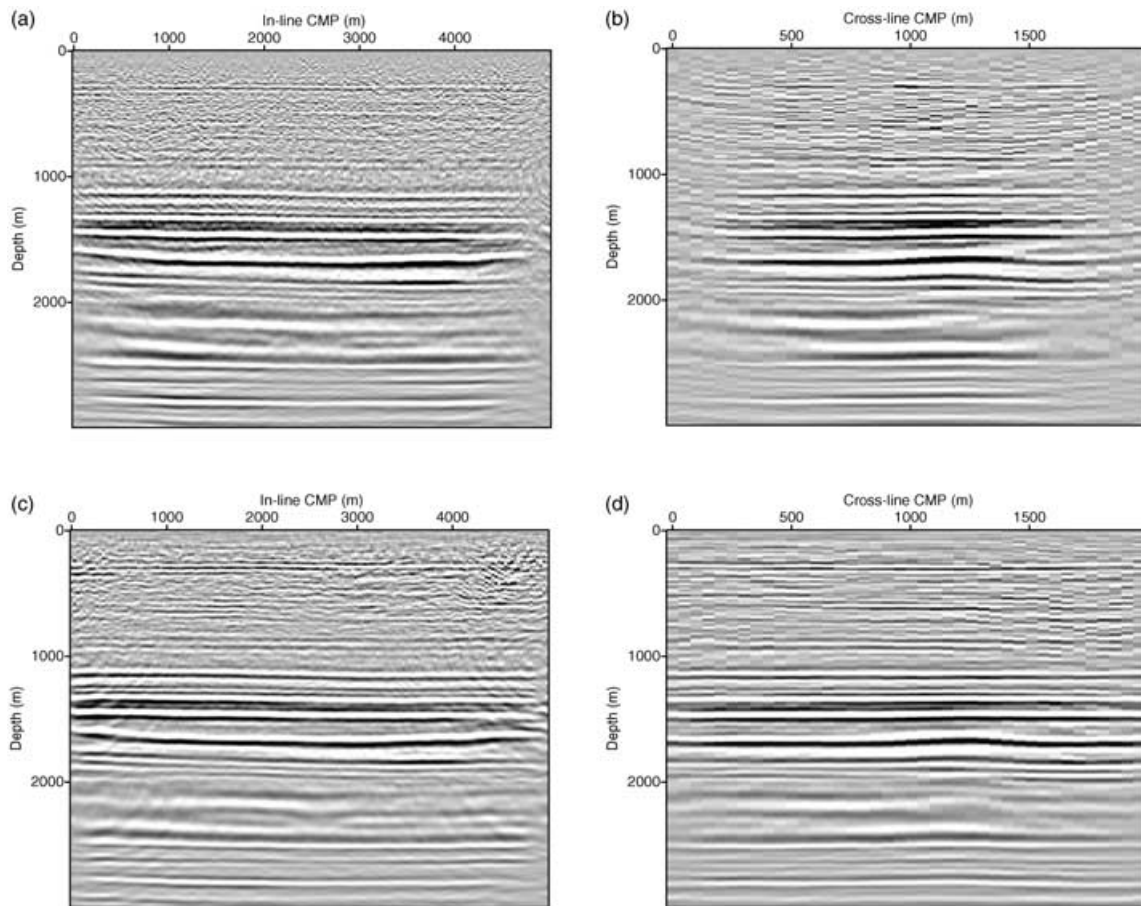


Figure 17 (a) Cross-line #36 and (b) in-line #71 images of migrated 3D common-azimuth data without interpolation. (c) Cross-line #36 and (d) in-line #71 images of migrated 3D common azimuth data with interpolation.

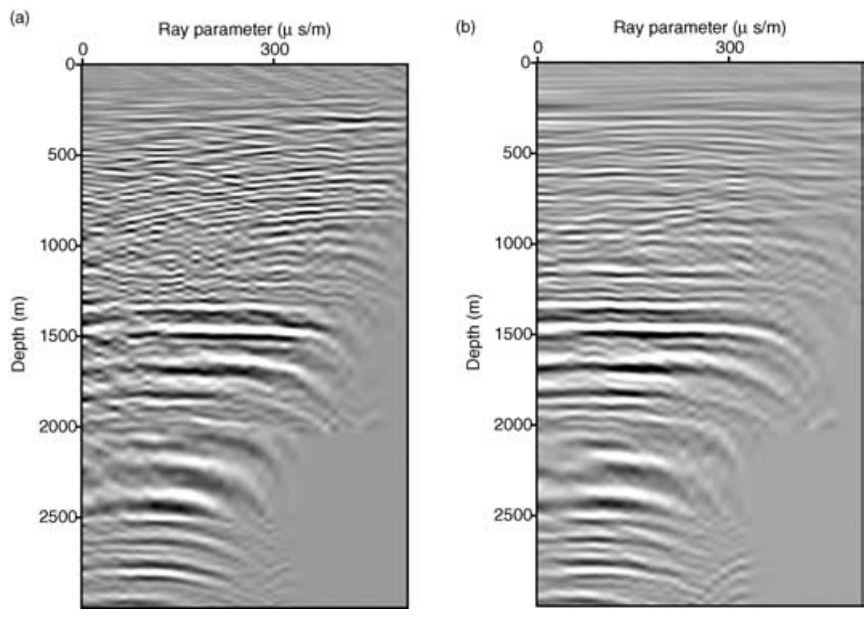


Figure 18 The common-image gathers obtained with (a) the undersampled data (original prestack volume) and (b) the reconstructed data.

## ACKNOWLEDGEMENTS

This study was funded by the sponsors of the Signal Analysis and Imaging Group at the University of Alberta and a grant from the National Sciences and Engineering Research Council of Canada. We also thank Dr Scott Cheadle (Veritas DGC Ltd, Calgary) for providing the Erskine data set. We also thank the reviewers who have helped to improve the quality of this paper.

## REFERENCES

- Biondi B. and Palacharla G. 1996. 3-D prestack migration of common-azimuth data. *Geophysics* **61**, 1822–1832.
- Cary P. 1997. High-resolution “beyond Nyquist” stacking of irregularly sampled and sparse 3-D seismic data. CSEG Annual Meeting, Calgary, Canada, Expanded Abstracts, 66–70.
- Claerbout J.F. 1985. *Imaging the Earth's Interior*. Blackwell Scientific Publications.
- Claerbout J.F. 1991. Principles of beyond-aliasing interpolation. 61st SEG meeting, Houston, USA, Expanded Abstracts, 1460–1464.
- Duijndam A.J.W., Schonewille M.A. and Hindriks C.O.H. 1999. Reconstruction of seismic signals, irregularly sampled along on spatial coordinate. *Geophysics* **64**, 524–538.
- Hanke M. 1995. Conjugate gradient type methods for ill-posed problems. In: *Pitman Research Notes in Mathematics*. Longman House.
- Hansen P.C. 1998. *Rank-deficient & Discrete Ill-Posed Problems: Numerical Aspects of Linear Inversion*. SIAM Monographs on Mathematical Modeling and Computation 4.
- Hestenes M. and Stiefel E. 1952. Methods of conjugate gradients for solving linear systems. *Journal of Research of the National Bureau of Standards* **49**, 403–436.
- Hindriks C.O.H. and Duijndam A.J.W. 2000. Reconstruction of 3-D seismic signals irregularly sampled along two spatial coordinates. *Geophysics* **65**, 253–256.
- Hugonnet P., Herrmann P. and Ribeiro C. 2001. High resolution Radon – a review. 63rd EAGE conference, Amsterdam, Netherlands, Extended Abstracts, IM-2.
- Kuehl H. and Sacchi M.D. 2003. Least-squares wave-equation migration for AVP/AVA inversion. *Geophysics* **68**, 262–273.
- Liu B. and Sacchi M.D. 2001. Minimum weighted norm interpolation of seismic data with adaptive weights. 71st SEG meeting, San Antonio, Texas, USA, Expanded Abstracts, 1921–1924.
- Liu B. and Sacchi M.D. 2003. Adaptive weighted minimum norm pre-stack interpolation. 65th EAGE conference, Stavanger, Norway, Extended Abstracts, D22.
- Marple S.L. 1987. *Digital Spectral Analysis with Applications*. Prentice-Hall, Inc.
- Mosher C.C., Foster D.J. and Hassanzadeh S. 1997. Common angle imaging with offset plane waves. 67th SEG meeting, Dallas, USA, Expanded Abstracts, 1379–1382.
- Priestly M.B. 1981. *Spectral Analysis and Time Series*. Academic Press, Inc.
- Prucha M., Biondi B. and Symes W. 1999. Angle domain common image gathers by wave-equation migration. 69th SEG meeting, Houston, USA, Expanded Abstracts, 824–827.
- Sacchi M.D., Ulrych T.J. and Walker C. 1998. Interpolation and extrapolation using a high-resolution discrete Fourier transform. *IEEE Transactions on Signal Processing* **46**, 31–38.
- Spitz S. 1991. Seismic trace interpolation in the F-X domain. *Geophysics* **56**, 785–794.
- Wang J., Kuehl H. and Sacchi M.D. 2003. Least-squares wave-equation AVP imaging of 3-D common azimuth data. 73rd SEG meeting, Dallas, USA, Expanded Abstracts, 1039–1042.
- Zwartjes P.M. and Duijndam A.J.W. 2000. Optimizing reconstruction for sparse spatial sampling. 70th SEG meeting, Calgary, Canada, Expanded Abstracts, 2161–2165.